ingegneria sismica
International Journal of Earthquake Engineering
Anno XLIII - Num. 3 - 2026

Model-Assisted Simulation of Cu(II) and Pb(II) Co-Adsorption by Sodium Alginate–Biochar Composite Materials

Haoyu Shan[1,*]

[1] College of Resources and Environment, Jilin Agricultural University, Changchun 130118, P.R. China

SUMMARY: *Addressing the challenge that traditional isotherm models struggle to reliably describe the competitive adsorption of Cu(II)/Pb(II) mixed ions in formed composite adsorbents,this study constructs a batch adsorption experimental matrix for sodium alginate–biochar composite materials and proposes a Physically Constrained Competitive Adsorption Graph Attention Network (PI-CGAT) to predict and interpret the adsorption capacity, removal efficiency, equilibrium concentration, and Pb(II)/Cu(II) selectivity coefficient in the Cu(II)/Pb(II) binary system.The experimental matrix covers pH 3.0–6.0, contact times of 5–360 min, temperatures of 288–318 K, initial metal ion concentrations of 20–200 mg/L, adsorbent dosages of 0.5–2.0 g/L, and SA/BC mass ratios of 1:1–3:1.PI-CGAT adsorbed Cu(II), Pb(II),carboxyl, hydroxyl, and C–O sites; Ca-crosslinked sodium alginate sites; the mesoporous region of biochar; the aromatic carbon region; mineral ash sites; and pH-regulated surface charge as heterogeneous graph nodes, and represented complexation, ion exchange, pore-associated adsorption, mineral binding, and Cu/Pb competition as edge relationships.At pH 5.5, C_0,Cu = C_0,Pb = 100 mg/L,a dosage of 1.0 g/L, and a contact time of 240 min, the equilibrium adsorption capacities of SA–BC 2:1 for Cu(II) and Pb(II) were 58.27 ± 1.61 mg/g and 88.76 ± 2.22 mg/g, respectively, corresponding to removal efficiencies of 58.27% and 88.76%.In the stoichiometric binary system, the Pb(II)/Cu(II) selectivity coefficient reached 5.63.Model testing results show that the PI-CGAT model has prediction R^2 values of 0.947 and 0.958 for q_Cu and q_Pb, respectively, with RMSEs of 4.86 mg/g and 5.54 mg/g. Ablation results indicate that removing competing edges increases the overall RMSE by 45.29%, while removing physical constraints increases the overall RMSE by 22.79%.Attention weights show that at pH 5.5, the weights of Pb(II) for the –COOH and Ca-crosslinked sites were 0.36 and 0.22, respectively, while the weight of Cu(II) for the mesopore domain rose to 0.20.The results indicate that PI-CGAT can characterize Cu(II)/Pb(II) site competition while maintaining the physical boundaries of adsorption, providing an interpretable simulation tool for the structural design of composite adsorbents and the optimization of treatment conditions for mixed heavy metal wastewater.*

KEYWORDS: *Sodium alginate-biocarbon composite; Cu(II)/Pb(II); Competitive adsorption; Graph attention network; Physically constrained model*

1 Introduction

Copper- and lead-contaminated wastewater in electroplating, metallurgy, mine drainage, battery manufacturing, electronic material processing, etc., has all been monitored. Although

---

*13179136257@163.com

https://doi.org/10.65102/is20261275

Cu(II) is required for life in moderate amounts, if it is present in the discharged water at high concentrations, it may damage microbial life and lead to problems for the aquatic environment; Pb(II) accumulates in living tissues more easily than Cu(II) and can harm the central nervous system, kidneys and even affect the growth of children at very low levels. These two ions often coexist in actual industrial wastewater, and the adsorption behavior of a single metal ion cannot directly explain site competition, mass transfer differences, or selective adsorption in mixed systems. Therefore, adsorption studies of Cu(II)/Pb(II) mixed ions need to address simultaneously whether the material has a high adsorption capacity, how the two ions compete for active sites, whether changes in experimental conditions affect the order of selectivity, and whether models can accurately predict adsorption behavior based on a limited number of experimental samples.

Sodium alginate-based adsorbents are suitable for the removal of heavy metal ions because they have carboxyl and hydroxyl groups on the molecular chain, and thus can bind multivalent metal ions through coordination, ion exchange and other forms of interaction [1-3]. Calcium-crosslinked sodium alginate can also form a three-dimensional gel network to help shape adsorbents, facilitate solid-liquid separation and reuse. However, sodium alginate gels alone have shortcomings in terms of mechanical strength, pore collapse and a low mass transfer rate; therefore, adsorption capacity is reduced in high-ionic-strength or complex-water environments. Biochar has an aromatic carbon skeleton, a porous structure, mineral components in its ash, and oxygen-containing functional groups; it can participate in metal ion immobilization via surface complexation, cation exchange, pore filling and mineral precipitation [4, 5]. Embedding biochar in sodium alginate gel introduces multi-scale pore channels and carbon-based adsorption interfaces, maintains the advantages of shape retention and separation, and thus improves mass transfer conditions and site diversity for the composite material.

Previous studies have shown that sodium alginate/biochar composites are suitable for the removal of Cu(II), Pb(II) and other inorganic pollutants. H_2O_2-modified peanut shell biochar/alginate composite beads have been used for Cu(II) removal; it has been shown that surface oxidation modification of biochar and gel formation can simultaneously enhance both adsorption capacity and separation performance [6]. Alginate composite hydrogel beads containing biochar have been applied to the adsorption of Cu^{2+} in both single-component and binary systems, and traditional kinetic and isotherm models can describe the equilibrium trends under local conditions [7]. For Pb(II), both MoS_2-loaded biochar/$CaCO_3$/alginate gel beads and recoverable biochar/alginate gel have exhibited excellent removal effects; related studies have pointed out that oxygen-containing sites, Ca-crosslinked structures and mineral components play important roles in Pb(II) fixation [8, 9]. These studies provide material support for using SA–BC composites in binary heavy metal adsorption; however, due to substantial differences among different material ratios, solution conditions and contaminant combinations, a single empirical model is difficult to establish for multivariate competitive scenarios.

The first problem in the Cu(II)/Pb(II) mixed system is competitive adsorption. Cu(II) and Pb(II) have different hydration radii, coordination preferences and hydrolysis behaviors; thus, their occupancy probabilities at carboxyl groups, hydroxyl groups, mineral ash and biochar defect sites are not the same. Increasing pH promotes carboxyl deprotonation and increases the surface negative charge density; however, too high a pH can lead to metal hydrolysis or precipitation interference. Increasing the dose enhances the general removal rate, but it may reduce q_e because the number of ion sites per unit mass is declining; although an increased initial concentration boosts the mass-transfer driving force, when Pb(II) exhibits a dominant site-occupancy effect, the incremental adsorption capacity for Cu(II) will be suppressed. Although the Langmuir, Freundlich and pseudo-second-order models can describe the capacity and equilibrium changes under localized experimental conditions, they are not suitable for addressing the combined impact of multivariate coupling, bimetallic competition and differences in material structure on the adsorption pathway [10-13].

Models of the adsorption behaviour based on data have been introduced. Machine learning has been used to predict the adsorption efficiency of heavy metals by biochar, optimise preparation conditions and screen high-dimensional variables [14-20]. Although such models have improved the predictive performance of complex adsorption systems, most of these methods still use tabular features as input and primarily learn statistical mappings between variables and outcomes. For Cu(II)/Pb(II) coexistence systems, simply concatenating pH, temperature, concentration and other material characteristic indices in a feature vector fails to capture the interaction mechanisms of metal ions, functional groups, pore structure, competition, etc., in an explicit manner. It is also unable to ensure that the prediction results satisfy the principles of mass conservation, non-negative adsorption capacities and adsorption equilibrium.

Graph Neural Networks are good at handling material and adsorption problems with relational structures. Graph Attention Networks can learn different weights for different adjacent nodes and are therefore suitable for dealing with non-uniform connection strengths among heterogeneous nodes [21]; physics-informed neural networks introduce physical laws as training constraints to improve the generalisation ability of models in cases of small sample sizes and incomplete data [22]; and research on material adsorption has already applied crystal graph convolutions and graph neural networks to predict adsorption capacity or adsorption energy, showing that adsorption objects can be represented as graph structures [23, 24]. Existing graph models mainly focus on crystals, metal surfaces or gas adsorption systems, and there is still a lack of integration with the competitive adsorption of heavy metals in aqueous phase, composite adsorbents and batch experimental data.

Given the above problems, this study investigates the adsorption behaviour of Cu(II)/Pb(II) mixed ions by sodium alginate–biochar composites and presents experimental data organisation and model-coupled simulations. Batch adsorption data under various conditions, including pH, contact time, temperature, adsorbent dosage, initial concentration ratio, and SA/BC mass ratio, were obtained to calculate the specific adsorption capacity, removal efficiency, equilibrium concentration, and Pb(II)/Cu(II) selectivity coefficient for Cu(II) and Pb(II). Characterization results such as BET, FTIR, zeta potential and pH_pzc were used to build the material structure input, and for the model, this study developed a Physically Constrained Competitive Adsorption Graph Attention Network (PI-CGAT) that represented Cu(II), Pb(II), oxygen-containing functional groups, Ca cross-linking sites, biochar pore structure and mineral sites as heterogeneous graph nodes; depicted complexation, ion exchange, pore diffusion, pH regulation and Cu/Pb competition as edge relationships; and introduced non-negativity, mass conservation and capacity boundary constraints in the prediction head. A relatively simple simulation system will be constructed in this paper to address all the factors in the experiment, including material structure and other binding processes.

2 Methods

The following are the locations of materials and model structures, along with experimental data pipelines. The hierarchical pore structure, oxygen-containing functional groups and Ca cross-linking network of the SA–BC composite form the basis of the adsorption site; PI-CGAT organises metal ions, sites and solution conditions into a competitive adsorption graph; and the batch adsorption experimental matrix provides a unified data interface for model training, baseline comparison and error analysis, as shown in Figures 1-3.

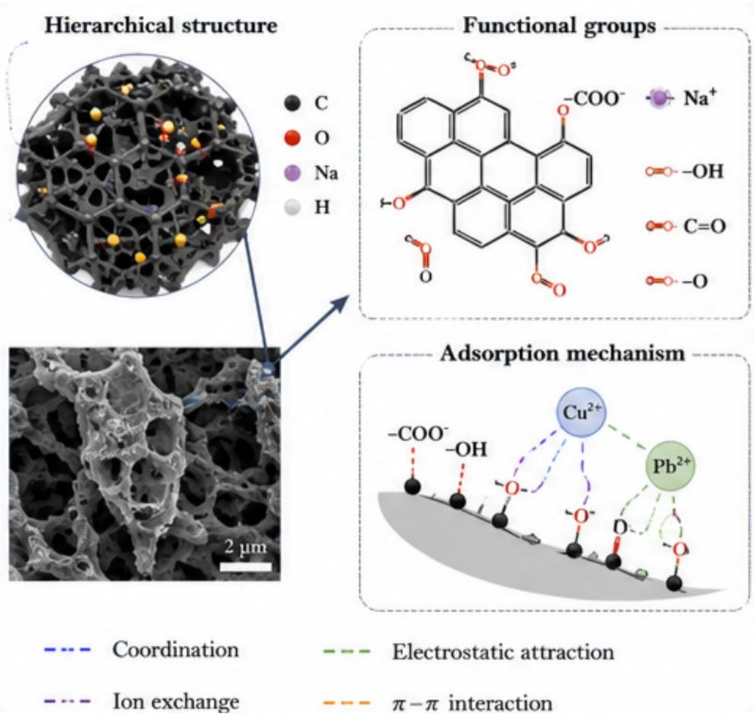

Figure 1: Material structure and Adsorption Mechanism

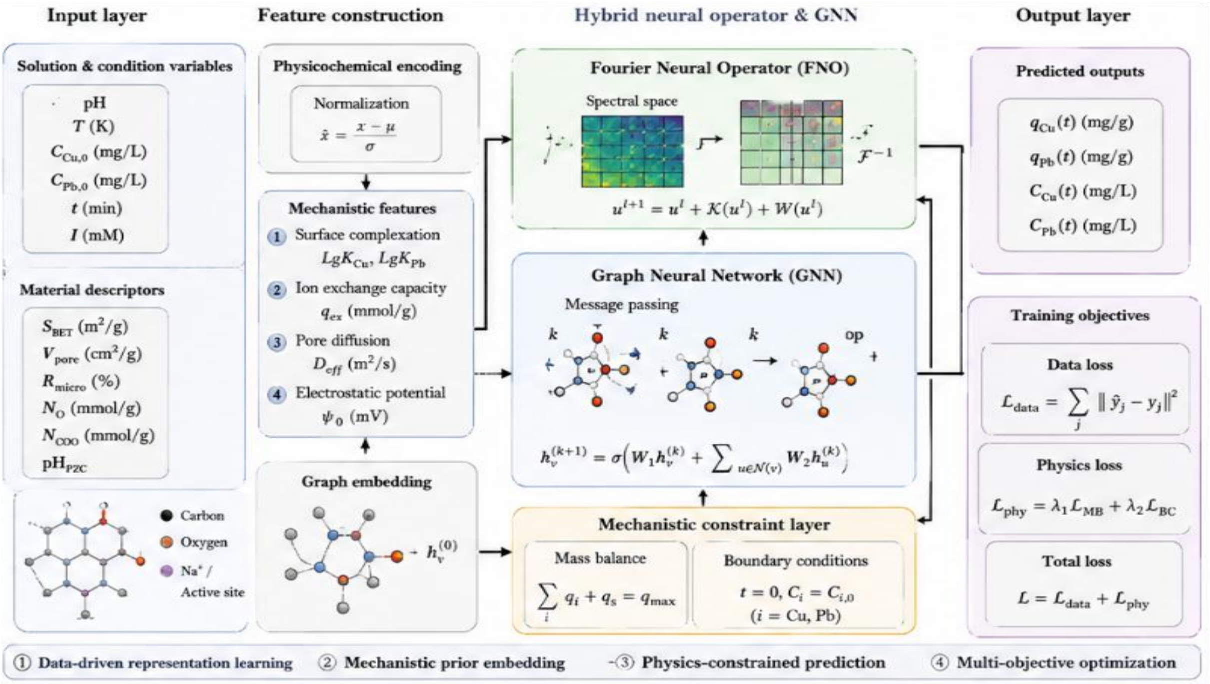

Figure 2: Architecture of the Algorithm-Mechanism Coupled Model

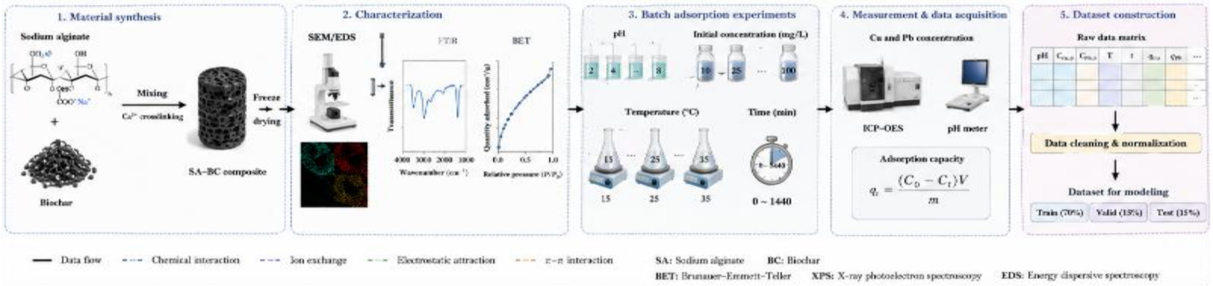

Figure 3: Experimental Workflow and Data Pipeline

2.1 Material Structure, Active Sites, and Characterization Descriptors

SA-BC composite material is a network of sodium alginate gel and a pore structure of biochar. Sodium alginate has -COO⁻, -OH, and Ca^{2+} cross-linking sites, which are mainly involved in coordination, complexation and ion exchange; Biochar has mesoporous channels, aromatic carbon regions, ash mineral sites, and defect edges, and mainly influences diffusion pathways, surface complexation and mineral binding. As shown in Figure 1, the hierarchical pore structure, functional group distribution and ion adsorption interfaces collectively correspond to material descriptors and can be used as inputs for the subsequent model.

A drop-wise cross-linking method was employed for material preparation. Wash, dry and sieve; then, at a mass ratio of 1:1, 2:1 and 3:1, add biochar powder to sodium alginate solution and dropwise add $CaCl_2$ solution to form cross-linked gel beads. After drying, the materials were labelled SA–BC 1:1, SA–BC 2:1 and SA–BC 3:1. BET specific surface area, total pore volume, mean pore diameter, pHpzc, zeta potential at pH 5.5, FTIR peak shift, Ca content and ash content were characterisation parameters. BET and pore structure parameters were employed to study mass transfer space; FTIR peak shifts reflected the intensity of participation by carboxyl, hydroxyl and C–O sites after metal binding; and Ca content described the ion exchange potential of cross-linking sites.

As shown in Table 1, the SBET of BC is 286.7 m²/g; thus, it possesses a large external surface area and many internal pore interfaces. After composite formation, with an increase in the ratio of sodium alginate, the specific surface area decreases; for SA-BC 2:1, it is 96.8 m²/g, and although some pore channels remain, SA-BC 3:1 exhibits a reduced zeta potential of -34.2 mV due to enhanced surface negativity but has a small Vpore of only 0.071 cm³/g, indicating that the mass transfer space has been constricted. Based on all-round analysis of pore structure, Ca content and FTIR peak shifts, SA–BC 2:1 was chosen as the main simulation material.

Table 1: Characterization Data for Sodium Alginate-Biochar Composites as Model Inputs

Material	S_{BET} / $m^2 \cdot g^{-1}$	V_{pore} / $cm^3 \cdot g^{-1}$	D_{pore} / nm	pH_{pzc}	Zeta / mV	$\Delta\nu_{COOH}$ / cm^{-1}	$\Delta\nu_{OH}$ / cm^{-1}	Ca / wt.%	Ash / wt.%
BC	286.7	0.236	3.29	6.42	-18.6	6.4	8.1	0.21	9.6
SA–BC 1:1	138.4	0.142	4.11	5.38	-25.4	17.2	11.6	3.18	5.2
SA–BC 2:1	96.8	0.105	4.36	4.92	-30.8	22.5	13.8	4.62	3.9
SA–BC 3:1	62.5	0.071	5.04	4.61	-34.2	24.0	15.1	5.34	2.8

2.2 PI-CGAT Model Structure, Graph Construction, and Physical Constraints

PI-CGAT is a heterogeneous competitive adsorption graph for binary adsorption samples. As shown in Figure 2, the left input layer obtains solution variables, material descriptors, node embeddings and edge attributes; the central heterogeneous graph contains metal ion nodes, adsorption site nodes and pH control nodes; finally, the right prediction head simultaneously outputs adsorption capacity, removal rate, equilibrium concentration and selectivity coefficient. The core of this model is to convert tabular data into a graph structure that captures chemical relationships among different parts, and thus it is possible to explicitly express the competitive binding of Cu(II) and Pb(II) through edge weights and attention coefficients.

The three kinds of nodes in a graph are: The first type of node is a metal ion node, which includes Cu(II) and Pb(II); its attributes include initial concentration, ionic radius, hydration radius, valence state and reaction state with the solution pH. The second type of node is a site node, and among them are –COOH, –OH, C–O, Ca-crosslinked sites, mesopore domains, aromatic carbon domains, and mineral ash sites. The attributes of the nodes are the functional groups, pore structures and mineral components shown in Table 1. The third type are pH-responsive surface charge sites with a pH_pzc, zeta potential and proton competition strength.

Edge interactions are used to describe specific adsorption processes. Cu/Pb competitive edges link Cu(II) and Pb(II), and edge attributes include C_0, Cu/C_0, Pb ratios, total metal loading and site-specific competition intensity. Ion–functional group edges are related to complexation and coordination at carboxyl, hydroxyl and C–O sites; ion–Ca site edges show exchange behaviour at Ca^{2+} cross-linking sites; ion–biochar site edges represent the contributions of mesoporous regions, aromatic carbon regions and mineral ash sites to diffusion and binding; and pH–site edges describe the regulation of functional group dissociation and surface charge state by pH.

The input layer standardizes continuous variables, while categorical variables are transformed into low-dimensional vectors via an embedding layer. The model employs two graph attention layers, each with 4 attention heads, a hidden dimension of 64, and a dropout rate of 0.10.The attention layers jointly calculate neighborhood contributions based on node representations and edge attributes, enabling the distinction of Pb(II)'s preference for carboxyl and Ca-binding sites, Cu(II)'s response to mesoporous regions and mineral sites, and the phenomenon of increased weighting of mineral ash sites under boundary pH conditions.The prediction head consists of two fully connected layers, outputting $q_{\mathrm{Cu}}, q_{\mathrm{Pb}}, R_{\mathrm{Cu}},\ R_{\mathrm{Pb}}, C_{e,\mathrm{Cu}},\ C_{e,\mathrm{Pb}}\ , and\ S_{\mathrm{Pb/Cu}}$.

2.3 Adsorption Data Pipeline, Formula Definitions, and Evaluation Protocol

Figure 3 is the experimental workflow and data pipeline. Material preparation was followed by SEM/EDS, FTIR, BET and surface charge characterisation in sequence, and then batch adsorption experiments were conducted. Controlled variables in the binary adsorption experiments included pH, initial concentration, temperature, contact time and dosage; the measurement phase determined the equilibrium concentrations of Cu(II) and Pb(II); and data preparation cleaned and normalised the raw concentration matrix before dividing it into training, validation and test sets.

The batch adsorption matrix includes pH values of 3.0, 4.0, 5.0, 5.5 and 6.0; contact times are 5, 15, 30, 60, 120, 240 and 360 min; temperatures are 288, 298, 308 and 318 K; initial Cu(II) and Pb(II) concentrations are 20, 50, 100, 150 and 200 mg/L; and adsorbent dosages are 0.5, 1.0, 1.5 and 2.0 g/L. Three sets of parallel experiments were conducted under all conditions. A 70:15:15 split was used for the training, validation and test sets, and samples that were in parallel under the same experimental conditions were not distributed randomly among the subsets.

Table 2: Cu(II)/Pb(II) Binary Adsorption Experiment Matrix

Variable	Level or range	Unit	Model role
Initial Cu(II) concentration	20, 50, 100, 150, 200	mg/L	Cu input intensity and competitive load
Initial Pb(II) concentration	20, 50, 100, 150, 200	mg/L	Pb input intensity and competitive load
pH	3.0, 4.0, 5.0, 5.5, 6.0	—	Surface charge and proton competition
Contact time	5, 15, 30, 60, 120, 240, 360	min	Kinetic inputs
Temperature	288, 298, 308, 318	K	Thermodynamic conditions
Adsorbent dosage	0.5, 1.0, 1.5, 2.0	g/L	Solid-liquid ratio
SA/BC mass ratio	1:1, 2:1, 3:1	—	Material structure descriptor
Replicate number	3	—	Error estimate
Detection object	Ce,Cu, Ce,Pb	mg/L	Concentration detection output
Supervised targets	$q_{\text{Cu}}, q_{\text{Pb}}, R_{\text{Cu}}, R_{\text{Pb}}, C_{e,\text{Cu}}, C_{e,\text{Pb}}, S_{\text{Pb/Cu}}$	—	Model prediction targets

$$q_i = \frac{(C_{0,i} - C_{e,i})V}{m}, \quad i \in \{\text{Cu(II)}, \text{Pb(II)}\} \tag{1}$$

Equation (1) is used to calculate the adsorption amount per unit mass of ions i. q_i represents the adsorption amount of Cu(II) or Pb(II), $C_{0,i}$ is the initial concentration of the corresponding ion, $C_{e,i}$ is the equilibrium concentration after adsorption, V is the volume of the solution, and$m$ is the mass of the adsorbent. This equation is derived from the law of conservation of mass and serves as the direct basis for calculating the two supervised targets q_{Cu} and q_{Pb}.

$$R_i = \frac{C_{0,i} - C_{e,i}}{C_{0,i}} \times 100\%, \quad i \in \{\text{Cu(II)}, \text{Pb(II)}\} \tag{2}$$

Equation (2) is used to calculate the removal rate of the ion i. R_i represents the removal ratio of Cu(II) or Pb(II) , while $C_{0,i}$ and $C_{e,i}$ denote the initial concentration and equilibrium concentration of the ion, respectively. This metric reflects the extent of reduction in metal ions in the solution under given dosing conditions and is used in conjunction with the adsorption capacity per unit mass to evaluate material performance.

$$S_{\text{Pb/Cu}} = q_{\text{Cu}}/C_{e,\text{Cu}} \tag{3}$$

Equation (3) is used to calculate the selectivity coefficient of Pb(II) relative to Cu(II) . A value of $S_{\text{Pb/Cu}}$ greater than 1 indicates that Pb(II) possesses a stronger apparent site-occupancy advantage in the binary system. This indicator is influenced by the adsorption capacities of Pb(II) and Cu(II), as well as the equilibrium concentration, and is used to characterize the strength of competitive adsorption sites.

$$\alpha_{ij}^{(k)} = \frac{\exp\left(\mathrm{LeakyReLU}\left(a_k^{T}[W_k h_i \| W_k h_j \| e_{ij}]\right)\right)}{\sum_{l \in \mathcal{N}_i} \exp\left(\mathrm{LeakyReLU}\left(a_k^{T}[W_k h_i \| W_k h_l \| e_{il}]\right)\right)} \tag{4}$$

Equation (4) is used to calculate the attention coefficient for the connection from nodej to node$i$ in the th attention head (k). Here, h_i and h_j denote the target node and the neighboring node, respectively; e_{il} is the edge attribute vector; W_k is the learnable transformation matrix; a_k is the attention vector; and $\mathcal{N}_i$ is the neighborhood set of node i. This equation enables the model to assign weights to different action pathways based on metal ion type, site type, pH partition, and concentration ratio.

$$\mathcal{L} = \mathcal{L}_{\mathrm{sup}} + \lambda_m \mathcal{L}_{\mathrm{mass}} + \lambda_c \mathcal{L}_{\mathrm{cap}} + \lambda_n \mathcal{L}_{\mathrm{nonneg}} + \lambda_s \mathcal{L}_{\mathrm{smooth}} \tag{5}$$

Equation (5) represents the total loss function of the PI-CGAT. $\mathcal{L}_{\mathrm{sup}}$ denotes the supervised prediction error, $\mathcal{L}_{\mathrm{mass}}$ represents the mass conservation penalty term, $\mathcal{L}_{\mathrm{cap}}$ denotes the capacity boundary penalty term, $\mathcal{L}_{\mathrm{nonneg}}$ represents the non-negativity constraint term, and $\mathcal{L}_{\mathrm{smooth}}$ denotes the kinetic smoothing term. λ_m, λ_c, λ_n, and λ_s are the weight coefficients for the corresponding constraints. This function prevents the model from generating predictions with negative adsorption amounts, negative equilibrium concentrations, values exceeding capacity boundaries, or abnormal oscillations over time.

The baseline models are Langmuir/Freundlich fitting, pseudo-second-order kinetic fitting, SVR, Random Forest, XGBoost, and MLP, and all models use the same training, validation and test sets. The four are R^2, RMSE, MAE and MAPE. Ablation models include removing the graph attention layer, removing physical constraints, removing the Cu/Pb competition edge, and using an MLP with only the same input variables.

3 Results and Discussion

3.1 Effects of pH, Contact Time, and Concentration Ratio on Binary Adsorption Behavior

The first two sets of responses to pH and contact time were analyzed for binary adsorption behaviour. The main experimental conditions were set as SA–BC 2:1, C_0,Cu = C_0,Pb = 100 mg/L, dosage of 1.0 g/L, and temperature of 298 K. pH and contact time jointly affect the extent of proton competition, surface charge, functional group dissociation and diffusion; therefore, they were chosen as the primary control variables for the kinetic data, as shown in Figure 4.

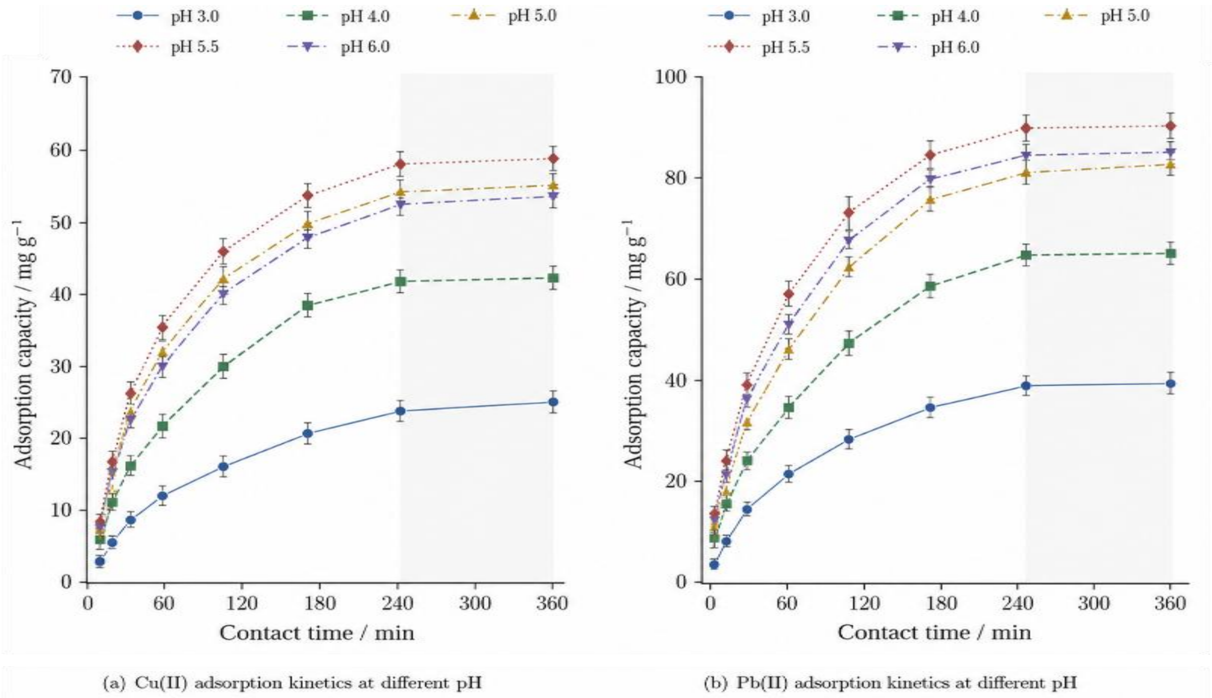

Figure 4: Effect of pH and contact time on adsorption capacity for the Cu(II)/Pb(II) binary system.

As shown in Figure 4, the adsorption capacities of both Cu(II) and Pb(II) increased with time and then reached a plateau, but there were considerable differences in the growth rates and plateau values of the two ions. At pH 3.0, q_Cu and q_Pb were only 25.06 mg/g and 38.35 mg/g after 240 min, respectively; thus, competition from H^+ for carboxyl and hydroxyl sites at low pH inhibited metal ion binding. When the pH was raised to 5.5, q_Cu and q_Pb reached 58.27 mg/g and 88.76 mg/g after 240 min, respectively, showing an increase of 132.52% and 131.45% compared with pH 3.0. At pH 6.0, both q_Cu and q_Pb at 240 min had decreased to 54.84 mg/g and 84.48 mg/g, respectively, which indicates that under boundary pH conditions, the trend of metal hydrolysis and the increasing complexity of surface reactions began to weaken the growth of effective adsorption.

Pb(II) was greater than Cu(II) at all pH values, and at pH 5.5 and 240 min, the adsorption capacity of Pb(II) was 30.49 mg/g higher than that of Cu(II). The above results are consistent with the strong coordinating tendency of Pb(II) for carboxyl and Ca cross-linking sites. The concentration ratio also affects the competition results in the binary system. As shown in Figure 5, the qe values for Pb(II) and Cu(II) are generally higher under the same concentration conditions. When C_0,Cu = C_0,Pb increases from 20 mg/L to 200 mg/L, qPb rose from 17.1 mg/g to 145.6 mg/g, and qCu increased from 13.2 mg/g to 92.4 mg/g.

As shown in Figure 5, the selectivity coefficient was 5.63 at a total ionic load of 100/100 mg/L, and then dropped to 3.12 when the total ionic load was increased to 200/200 mg/L; thus, although Pb(II) still dominates under this condition and the total ionic load has reached the maximum capacity of the material, a reduced number of available sites has led to a lower selectivity. At non-equimolar conditions, SPb/Cu decreased to 1.21 at 100/20 mg/L, indicating that the shortage of Pb(II) weakened its apparent selectivity, and at 50/100 mg/L, SPb/Cu was 4.38; therefore, as the amount of Pb(II) increased, it was more likely to be adsorbed at carboxyl and Ca-coordinating sites.

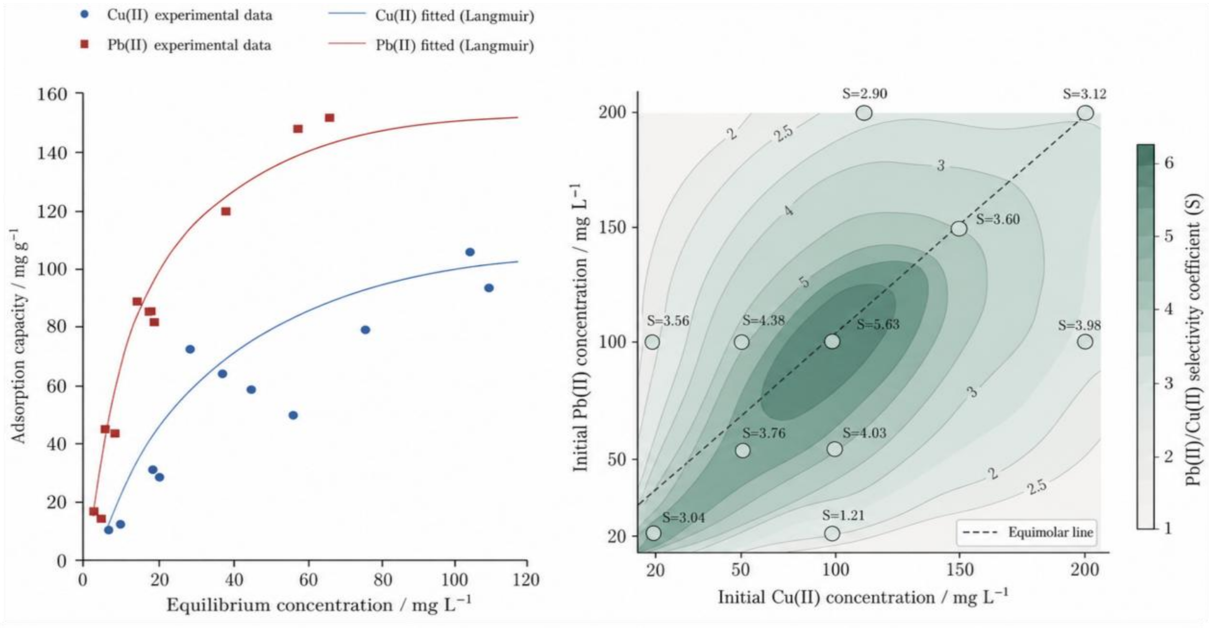

(a) Competitive adsorption isotherms

(b) Selectivity distribution in the binary Cu/Pb system

Figure 5: Competitive Adsorption Isotherms and Selectivity Distributions

3.2 PI-CGAT Predictive Performance, Baseline Comparison, and Ablation Analysis

Set up the experimental boundaries and competitive adsorption data, and then use an independent test set to assess the predictive ability of PI-CGAT for qCu and qPb. Traditional isotherm models only use equilibrium concentration information; machine learning models are tabular variables, and PI-CGAT also incorporates ion nodes, site nodes, competitive edges, and physical constraints. As shown in Figure 6, PI-CGAT has an R^2 of 0.947 for qCu and 0.958 for qPb, with RMSEs of 4.86 mg/g and 5.54 mg/g, respectively.

PI-CGAT outperformed XGBoost in reducing the RMSE for qCu by 21.74% and for qPb by 24.63%; it also reduced the RMSEs of qCu and qPb compared with MLP by 29.97% and 29.96%, respectively. The RMSEs of the traditional Langmuir/Freundlich models for qCu and qPb were 10.86 mg/g and 12.94 mg/g, respectively, and the main reasons for these errors were non-equimolar competition conditions and pH partitioning effects. Based on the above analysis, a single-equilibrium model can only explain local adsorption amounts and is not suitable for multivariate competition problems.

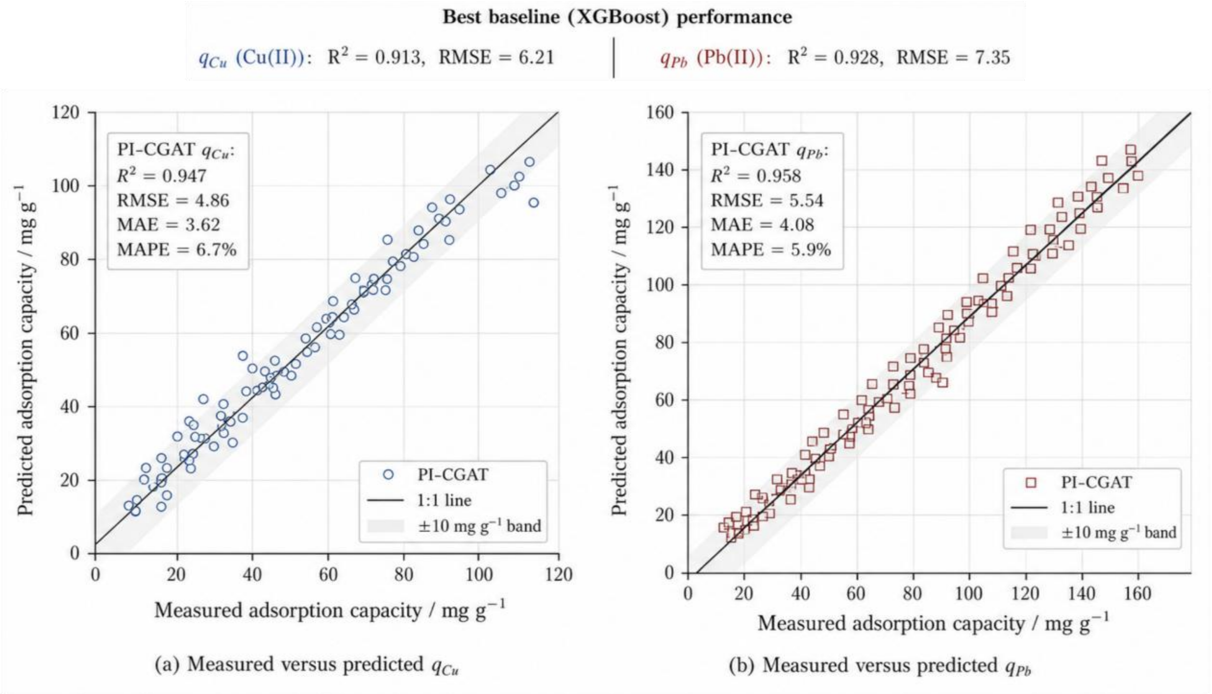

(a) Measured versus predicted q_{Cu}

(b) Measured versus predicted q_{Pb}

Figure 6: Performance of Adsorption Capacity Prediction by PI-CGAT and Others. Baseline Models

Figure 7 is also the ablation results. The mean RMSE of the full PI-CGAT is 5.20 mg/g. After removing the graph attention layer, the average RMSE increased to 6.75 mg/g and rose by 29.81%; after removing the physical constraints, the average RMSE was 6.39 mg/g and increased by 22.79%; and finally, after removing the Cu/Pb competitive edge, the average RMSE was 7.56 mg/g and rose by 45.29%. Notably, the RMSE for q_Pb increased from 5.54 mg/g to 8.43 mg/g; therefore, it can be inferred that competitive edge is a more sensitive structural term in the prediction of this binary system.

The adsorption capacity of Pb(II) is affected by the initial concentration of Cu(II), site saturation, and the occupancy of Ca-coordinating sites simultaneously. If the model only adds the combined concentration features, it may fail to account for the special binding characteristics of Pb(II) compared with other concentrations. The reasons for this limitation in the current model are: 1) Graph structures do not explicitly consider non-uniform interactions among Cu(II), Pb(II), and other sites; 2) Physical constraints are unable to restrict mass conservation violations and negative predictions at high concentrations.

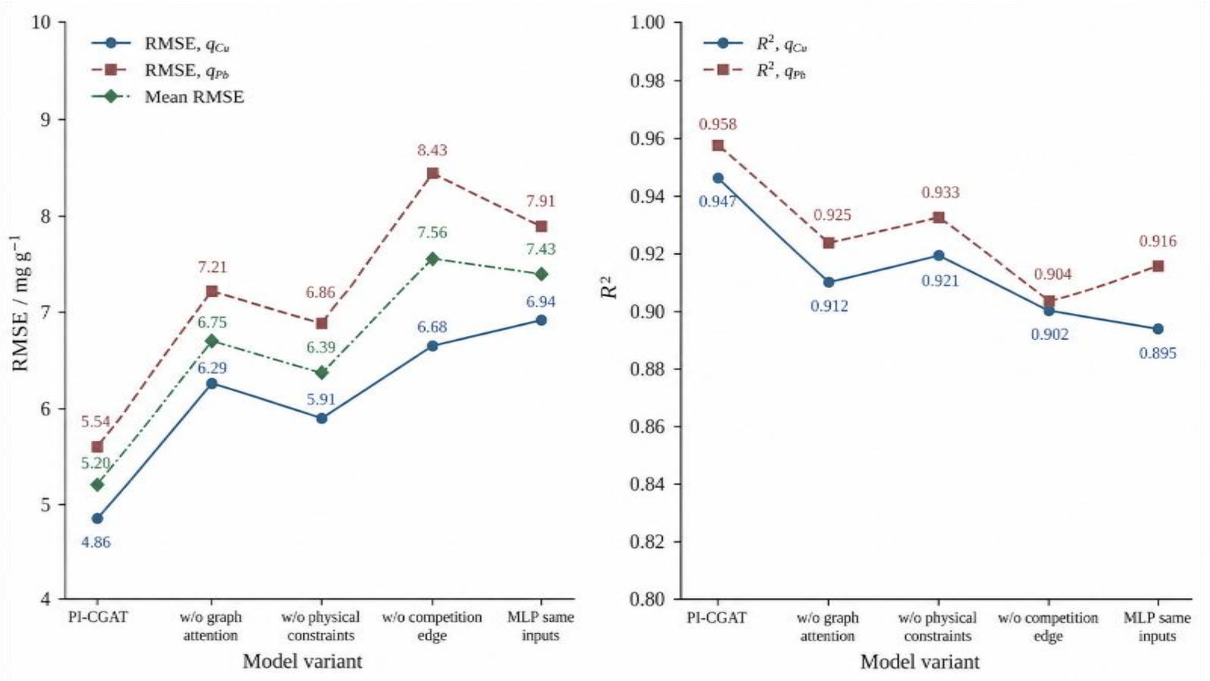

(a) RMSE comparison among ablation variants

(b) R^2 comparison among ablation variants

Figure 7: Ablation analysis of Graph Attention, Physical Constraints and Competing Edges

Table 3 shows the results of several models in the competition for adsorption simulation.

Table 3: Comparison of Performance among Different Models in Competitive Adsorption Simulations

Model	Input form	Competition representation	Physical constraint	Best Target Performance	Main limitation
Langmuir/ Freundlich	C_e and q_e	Missing	Capacity fit	q_{Pb} R^2 = 0.826	Difficult to describe binary competition
Pseudo-second-order	t and q_t	Missing	Kinetic fitting	Used for kinetic curves	Cannot account for the effect of concentration ratios
SVR	Table variables	Implicit	Missing	q_{Pb} R^2 = 0.871	Sensitive to scale and kernel parameters
Random Forest	Tabular variables	Implicit	Missing	q_{Pb} R^2 = 0.901	Limited generalization ability
XGBoost	Tabular variables	Implicit	Missing	q_{Pb} R^2 = 0.928	Insufficient physical consistency
MLP	Table variables	Implicit	Missing	q_{Pb} R^2 = 0.916	Missing ion-site structure
PI-CGAT	Heterogeneous adsorption plot	Explicit Cu/Pb competitive edge	Mass conservation, non-negativity, capacity boundary, kinetic smoothing	q_{Pb} R^2 = 0.958	Depends on structured descriptors

As shown in Table 3, the three main differences among the traditional adsorption models, conventional machine learning models and PI-CGAT are input information, representation of competitive relationships and physical consistency. Langmuir/Freundlich only need to obtain the equilibrium concentration and equilibrium adsorption capacity for capacity fitting, with an R^2 value of 0.826 for qPb. It can provide adsorption capacity trend information in a single equilibrium interval, but it lacks an expression for competing sites under Cu/Pb coexistence conditions. The pseudo-second-order model takes contact time and instantaneous adsorption capacity as inputs, is suitable for describing quasi-equilibrium processes in kinetic curves, but its structure does not include initial concentration ratios, material characterization variables, or ionic competition terms, and therefore cannot explain changes in Pb(II) selectivity between equimolar and non-equimolar systems.

A tabular variable model can be used to include pH, temperature, initial concentration, dosage and material descriptors to improve the prediction accuracy over that of traditional fitting models; the R^2 values for qPb using SVR, Random Forest, XGBoost and MLP were 0.871, 0.901, 0.928 and 0.916, respectively. Among them, XGBoost was the best-performing baseline model in the table-based model group; however, it could not demonstrate a superior advantage over PI-CGAT in variable concatenation, and constraints on ion nodes, site nodes, and edge relationships were absent. PI-CGAT achieved an R^2 value of 0.958 for qPb and, by adding these constraints (mass conservation, non-negativity, capacity limits and kinetic smoothing), improved this value by 0.030 compared with XGBoost. This result shows that the error in binary adsorption prediction is mainly due to the lack of competitive site information, rather than an inability of nonlinear fitting. PI-CGAT uses structured descriptors; therefore, in the future application to real wastewater, supplementary data on coexisting ions, dissolved organic matter, and material changes under recycling will still need to be obtained.

3.3 Attention Explanation, Error Distribution, and Model Applicability Boundaries

The graph attention weights of PI-CGAT can be employed to explain the competition among Cu(II) and Pb(II) at different pH values for adsorption sites. Under moderate concentration conditions in the test set of this study, we extracted the average attention weights and summarized them by metal ion and adsorption site, as shown in Figure 8. At pH 3.0, 5.5, and 6.0, the attention weights of Pb(II) for -COOH were 0.29, 0.36, and 0.31, respectively; these were all higher than those of Cu(II). At pH 5.5, the weight of Pb(II) for the Ca-crosslinked site was 0.22, higher than that of Cu(II) at 0.13, and thus it was determined that the Ca-crosslinked sodium alginate sites were a significant source of Pb(II) competition.

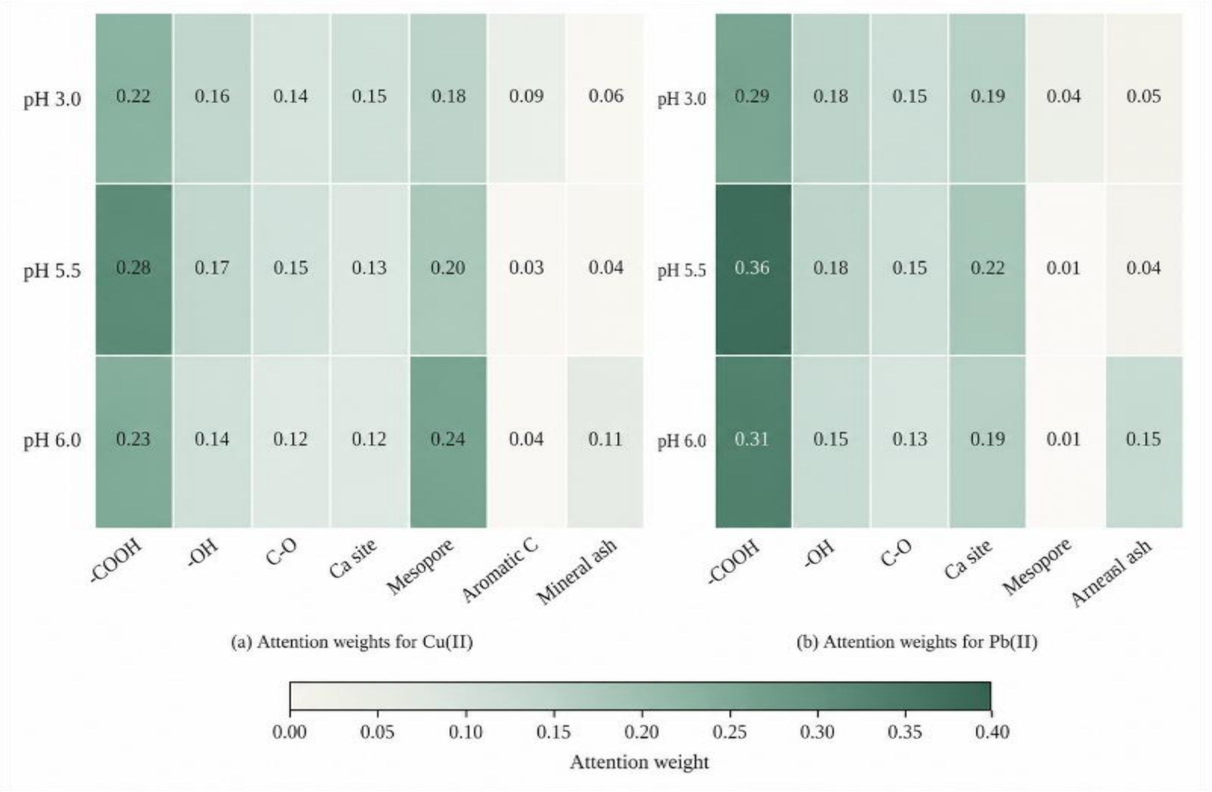

(a) Attention weights for Cu(II)

(b) Attention weights for Pb(II)

Figure 8: Weight Distribution of Cu(II)/Pb(II) Competitive Adsorption

The distribution of attention for Cu(II) is relatively spread out; at pH 5.5, its weight in the mesopore domain is 0.20, and it increases to 0.24 at pH 6.0, suggesting that the predicted results for Cu(II) are more dependent on pore structure and diffusion-related sites. At pH 6.0, the weights for the mineral ash site increase for both ions: Pb(II) rises from 0.04 at pH 5.5 to 0.15, and Cu(II) increases from 0.04 to 0.11. Therefore, it can be seen that the effect of mineral elements and possible hydrolysis products on model prediction is stronger in the boundary pH region.

Figure 9 is the distribution of errors at different pH values and C_0,Cu/C_0,Pb ratios. The model error was at its minimum at pH 5.5 and C_0,Cu/C_0,Pb = 1.00, with absolute errors of 3.1 mg/g and 3.6 mg/g for qCu and qPb, respectively. This area is close to the training data, has good active sites, and shows a stable competitive relationship. At pH 3.0, the qPb error was greater than 6.8 mg/g for all three concentration ratios; that is to say, the proton competition under low-pH conditions weakened the stable occupation of carboxyl and Ca cross-linking sites by Pb(II), and thus the model could no longer distinguish between unadsorbed ions and weakly bound ions accurately.

At pH 6.0 and C_0, Cu/C_0, Pb = 4.00, the absolute errors of qCu and qPb reached 6.8 mg/g and 7.5 mg/g, respectively; thus, it can be determined that high Cu loading and a boundary pH simultaneously amplify extrapolation errors. Based on these results, the stable application range of PI-CGAT is restricted to pH 5.0-5.5 and moderate concentration ratios, and an increase in sample density or the addition of metal speciation constraints is required for use at low pH, high pH, and extreme Cu/Pb ratio conditions.

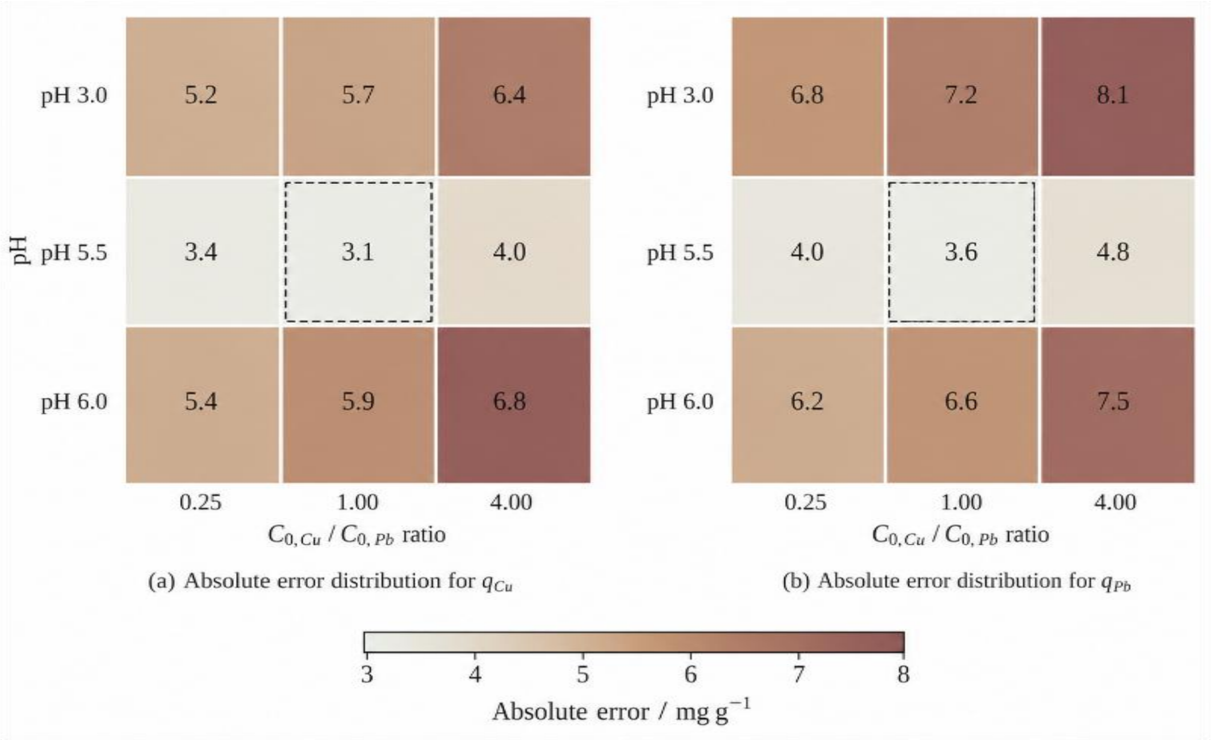

Figure 9: Distribution of Model Errors at Different pH and Cu/Pb Concentration Ratios

4 Conclusion

A simulation system based on material characterisation, batch adsorption experiments and a PI-CGAT model was constructed in this study to investigate the competitive adsorption behaviour of Cu(II)/Pb(II) mixed ions on SA-BC composites. Organise metal ions, adsorption sites, pH control nodes and competitive edges in a heterogeneous graph structure, and regulate prediction results through constraints on mass conservation, non-negativity, capacity limits, and kinetic smoothing.

First, SA–BC 2:1 has a relatively balanced structural profile of pores, Ca-crosslinked sites and oxygen-containing functional groups. Under conditions of pH 5.5, C_0,Cu = C_0,Pb = 100 mg/L, a dosage of 1.0 g/L, and 240 min, q_{Cu} and q_{Pb} reached 58.27 mg/g and 88.76 mg/g, respectively, and a Pb(II)/Cu(II) selectivity coefficient of 5.63. These results indicate that Pb(II) shows stronger competitive binding capacity at carboxyl and Ca cross-linking sites.

Second, PI-CGAT achieved R^2 values of 0.947 and 0.958 for the predictions of q_{Cu} and q_{Pb}, respectively, with RMSEs of 4.86 mg/g and 5.54 mg/g, and performed better than both traditional isothermal models and conventional machine learning models. Ablation analysis showed that the Cu/Pb competitive edge, the graph attention layer, and physical constraints all made significant contributions to prediction stability, and removing the competitive edge resulted in the largest increase in error.

Thirdly, attention weights and error distributions showed the model's limits of application. The main locations for Pb(II) were -COOH and Ca-crosslinked sites, and for Cu(II), the mesopore domain and mineral ash sites were more sensitive. The model has good stability in the pH 5.0-5.5 range and under moderate concentration ratios; otherwise, errors are relatively large at low pH, high pH, and at the extremes of the Cu/Pb ratio. In the future, some other ions, organic matter and recycling data from real industrial wastewater will be added to expand the model and enhance its application in all sorts of scenarios.

About the Author

Haoyu Shan The author was born in Yanbian, Jilin, China, in 2000. He obtained his bachelor’s degree from Jilin Agricultural University and is presently a graduate student at the College of Resources and Environment, Jilin Agricultural University. His research interests include renewable biomass utilization and the design of adsorption materials for water treatment.mail: 13179136257@163.com

References

[1] Elwakeel K.Z.; Ahmed M.M.; Akhdhar A.; et al. Recent advances in alginate-based adsorbents for heavy metal retention from water: a review. Desalination and Water Treatment, 2022, 272: 50–74. DOI: 10.5004/dwt.2022.28834.

[2] Gao X.; Guo C.; Hao J.; et al. Adsorption of heavy metal ions by sodium alginate-based adsorbents: a review and new perspectives. International Journal of Biological Macromolecules, 2020, 164: 4423–4434. DOI: 10.1016/j.ijbiomac.2020.09.046.

[3] Chen M.; Long A.; Zhang W.; et al. Recent advances in alginate-based hydrogels for the adsorption–desorption of heavy metal ions from water: a review. Separation and Purification Technology, 2025, 353: 128265. DOI: 10.1016/j.seppur.2024.128265.

[4] Wang J.; Wang S. Preparation, modification, and environmental application of biochar: a review. Journal of Cleaner Production, 2019, 227: 1002–1022. DOI: 10.1016/ j.jclepro.2019.04.282.

[5] Wang B.; Wan Y.; Zheng Y.; et al. Alginate-based composites for environmental applications: a critical review. Critical Reviews in Environmental Science and Technology, 2019, 49(4): 318–356. DOI: 10.1080/10643389.2018.1547621.

[6] Zhang L.; Li Q.; Zhu J.; et al. H_2O_2-modified peanut shell-derived biochar/alginate composite beads as a green adsorbent for the removal of Cu(II) from aqueous solution. International Journal of Biological Macromolecules, 2023, 240: 124466. DOI: 10.1016/j.ijbiomac.2023.124466.

[7] Park S.; Lee J.W.; Kim J.E.; et al. Adsorptive behavior of Cu^{2+} and benzene in single and binary solutions onto alginate composite hydrogel beads containing pitch pine-based biochar. Polymers, 2022, 14(17): 3468. DOI: 10.3390/polym14173468.

[8] He Y.; Jia X.; Zhou S.; et al. Separatable MoS_2-loaded biochar/$CaCO_3$/alginate gel beads for selective and efficient removal of Pb(II) from aqueous solution. Separation and Purification Technology, 2022, 303: 122212. DOI: 10.1016/j.seppur.2022.122212.

[9] Tao S.; Lu L.; Zhou T.; et al. Design of recoverable biochar/alginate gel and its removal performance for Pb(II) in water: Simulation and experiment. Journal of Molecular Liquids, 2024, 405: 125042. DOI: 10.1016/j.molliq.2024.125042.

[10] Shi W.; Yang J.; Guo Y.; et al. Mechanism of Pb(II) adsorption on a sodium alginate composite based on diatomite/crab shell biochar. Separation and Purification Technology, 2025, 378: 134732. DOI: 10.1016/j.seppur.2025.134732.

[11] Liu X.; Zhang Y.; Li H.; et al. Novel EDTA-chitosan/alginate porous composite beads for the simultaneous removal of Pb(II) and methyl blue from water. RSC Advances, 2025, 15: Article d5ra00940e. DOI: 10.1039/D5RA00940E.

[12] Wang X.; Liu Y.; Zhang H.; et al. Adsorption of Cu(II) and Pb(II) in aqueous solution by biochar derived from biomass waste. ACS Omega, 2025. DOI: 10.1021/acsomega.4c06837.

[13] Fan D.; Wang Y.; Chen J.; et al. Recent progress on the adsorption of heavy metal ions Pb(II) and Cu(II) by nanomaterials. Nanomaterials, 2024, 14(12): 1037. DOI: 10.3390/nano14121037.

[14] Yuan X.; Li J.; Lim J.Y.; et al. Machine learning for heavy metal removal from water: Recent advances and challenges. ACS ES&T Water, 2024, 4(3): 820–836. DOI: 10.1021/acsestwater.3c00215.

[15] Duan Q.; Yan P.; Feng Y.; et al. Machine learning-assisted evaluation of biochar adsorption performance for heavy metals. Frontiers of Environmental Science & Engineering, 2024, 18: 55. DOI: 10.1007/s11783-024-1815-4.

[16] Shen T.; Peng H.; Yuan X.; et al. Feature engineering for improved machine-learning-aided study of heavy metal adsorption on biochar. Journal of Hazardous Materials, 2024, 466: 133442. DOI: 10.1016/j.jhazmat.2024.133442.

[17] Yang H.; Liu X.; Liu Y.; et al. Revolutionizing biochar synthesis for enhanced heavy metal adsorption: Harnessing machine learning and Bayesian optimization. Journal of Environmental Chemical Engineering, 2023, 11(5): 110593. DOI: 10.1016/j.jece.2023.110593.

[18] Wang C.; Zhao Y.; Gao Y.; et al. Interpretable machine learning for predicting heavy metal removal and optimizing biochar characteristics. Journal of Water Process Engineering, 2024, 68: 106484. DOI: 10.1016/j.jwpe.2024.106484.

[19] Wei X.; Zhang Y.; Liu H.; et al. Machine learning insights in predicting heavy metal adsorption by biochar. Biochar, 2024. DOI: 10.1007/s42773-024-00304-7.

[20] Yaseen Z.M.; Alhalimi F.L. Heavy metal adsorption efficiency prediction using biochar properties: a comparative analysis for ensemble machine learning models. Scientific Reports, 2025, 15: 13434. DOI: 10.1038/s41598-025-96271-5.

[21] Veličković P.; Cucurull G.; Casanova A.; et al. Graph Attention Networks. International Conference on Learning Representations, 2018. arXiv: 1710.10903.

[22] Raissi M.; Perdikaris P.; Karniadakis G.E. Physics-informed neural networks: A deep learning framework for solving forward and inverse problems involving nonlinear partial differential equations. Journal of Computational Physics, 2019, 378: 686–707. DOI: 10.1016/j.jcp.2018.10.045.

[23] Jaffari Z.H.; Abbas A.; Umer M.; et al. Crystal graph convolution neural networks for fast and accurate prediction of the adsorption capacity of Nb_2CTx toward Pb(II) and Cd(II) ions. Journal of Materials Chemistry A, 2023, 11: 9009–9018. DOI:

10.1039/D3TA00019B.

[24] Pablo-García S.; Morandi S.; Vargas-Hernández R.A.; et al. Fast evaluation of the adsorption energy of organic molecules on metals via graph neural networks. Nature Computational Science, 2023, 3: 433–442. DOI: 10.1038/s43588-023-00437-y.

[25] Choudhary K.; DeCost B.; Chen C.; et al. Recent advances and applications of deep learning methods in materials science. npj Computational Materials, 2022, 8: 59. DOI: 10.1038/s41524-022-00734-6.